


## RESEARCH ARTICLE

WILEY

# Assessment of low-frequency aeroacoustic emissions of a wind turbine under rapidly changing wind conditions based on an aero-servo-elastic CFD simulation

Florian Wenz<sup>1</sup>  | Oliver Maas<sup>2</sup> | Matthias Arnold<sup>3</sup> | Thorsten Lutz<sup>1</sup> | Ewald Krämer<sup>1</sup>

<sup>1</sup>Institute of Aerodynamics and Gas Dynamics (IAG), University of Stuttgart, Stuttgart, Germany

<sup>2</sup>Institute of Meteorology and Climatology (IMUK), Leibniz University Hannover, Hannover, Germany

<sup>3</sup>Wobben Research and Development GmbH (WRD), Aurich, Germany

## Correspondence

Florian Wenz, Institute of Aerodynamics and Gas Dynamics (IAG), University of Stuttgart, Pfaffenwaldring 21, 70569 Stuttgart, Germany.  
Email: [wenz@iag.uni-stuttgart.de](mailto:wenz@iag.uni-stuttgart.de)

## Funding information

German Federal Ministry for Economic Affairs and Climate Action (BMWK), Grant/Award Number: FKZ 0325719F; University of Stuttgart

## Abstract

A meteorologically challenging situation that represents a demanding control task (rotational speed, pitch and yaw) for a wind turbine is presented and its implementation in a simulation is described. A high-fidelity numerical process chain, consisting of the computational fluid dynamics (CFD) solver *FLOWer*, the multi-body system (MBS) software *SIMPack* and the Ffowcs Williams-Hawkings code *ACCO*, is used. With it, the aerodynamic, servoelastic and aeroacoustic (<20 Hz) behaviour of a generic wind turbine during a meteorological event with strong and rapid changes in wind speed and direction is investigated. A precursor simulation with the meteorological model system *PALM* is deployed to generate realistic inflow data. The simulated strong controller response of the wind turbine and the resulting aeroelastic behaviour are analysed. Finally, the low-frequency sound emissions are evaluated and the influence of the different operating and flow parameters during the variable inflow is assessed. It is observed that the wind speed and, linked to it, the rotational speed as well as the turbulence intensity are the main influencing factors for the emitted low-frequency sound power of the wind turbine. Yawed inflow, on the other hand, has little effect unless it changes the operational mode to load reduction, resulting in a swap of the main emitter from the blades to the tower.

## KEYWORDS

aero-servo-elastic, CFD, low-frequency noise

## 1 | INTRODUCTION

Regardless of the complexity of the surrounding landscape, all wind turbines (WTs) have in common that they are operating in the atmospheric boundary layer. In this layer, a multitude of meteorological phenomena of completely different spatial and temporal scales occur, which interact with the WTs and ultimately define their operating conditions. The turbine control system ensures that the operation is constantly adapted to the prevailing conditions, mostly with the aim of achieving an optimal power output and, if necessary, with the aim of protecting the WTs from damage. The more transient a flow situation is, the more different operating points the WT is subject to and the more stress is put on the controllers. This can also cause the WT to run outside the intended operating range (off-design) if the controllers cannot adjust the WT fast enough. In

This is an open access article under the terms of the [Creative Commons Attribution](https://creativecommons.org/licenses/by/4.0/) License, which permits use, distribution and reproduction in any medium, provided the original work is properly cited.

© 2023 The Authors. *Wind Energy* published by John Wiley & Sons Ltd.

addition to performance losses and increased fatigue loads, this also has an influence on the aeroacoustic emissions. The development of a numerical process chain for the simulation of such a single event in the context of numerical forensics, for example, for WT manufacturers, opens up the possibility of counteracting problems already in the design phase. A framework from the wind field generation to the aero-servo-elastic simulation with CFD, taking into account the variability of rotational speed and the pitch and yaw controller, and a subsequent aero-acoustic evaluation is the goal.

## 1.1 | Wind turbine inflow and operational management

The wind conditions prevailing at a location result from the interaction of a variety of complex wind systems. The large-scale wind systems driven by the earth's climate zones are overlaid by small-scale wind systems due to local pressure differences, such as between sea and land or mountain and valley. The influence of ground roughness and the turbulent exchange of heat and moisture also affect the local flow field in the atmospheric boundary layer. An overview of atmospheric processes from macroscale (>1000 m) to microscale (<10 m) is given by Orlanski.<sup>1</sup> A WT can easily adapt to slow meteorological events thanks to its integrated control mechanisms. Fast changes with small amplitude, on the other hand, have hardly any influence on the operating point of the WT due to its large inertia, although fatigue loads and noise emissions increase as a result. However, events with large wind changes in a short time are potentially challenging for WTs.

There are many control strategies for WTs,<sup>2</sup> including those presented in Jonkman et al.,<sup>3</sup> Popko et al.<sup>4</sup> and Bak et al.<sup>5</sup> They feature the conventional approach for controlling power-production operation based on a generator-torque controller and a rotor-collective blade-pitch controller with a peak-shaving approach to reduce thrust force. Incorporating these controllers into multidisciplinary aerodynamic simulations is a challenge that is an ongoing research topic. Gözcü and Verelst<sup>6</sup> utilize the strongly coupled aero-servo-elastic wind turbine simulation tool HAWC2 to analyse the impact of the fidelity of the structural model. In their study, the aerodynamic solver uses the blade element momentum formulation and the structural solver is a multibody system (MBS) that contains a pitch and torque controller. Among other things, they show that the controller activity is also affected by the fidelity of blade modeling, demonstrating that aerodynamics, aeroelasticity and control are closely linked. However, if the aerodynamic loads are of primary interest, the fully resolved geometry of the blades should be considered. Li et al.<sup>7</sup> were among the first to present a simulation of a WT including computational fluid dynamics (CFD) of the rotor and tower aerodynamics, wind turbulence, elastic blades and pitch and torque control. They also state that their setup is able to handle yaw motion, but they did not apply it. Studies with CFD simulations of a resolved WT with an anemometer data driven yaw controller are not known to the authors and are not mentioned in the review of works on control strategies for yaw systems in Yang et al.<sup>8</sup> The work of Klein<sup>9</sup> is the only known study that numerically investigates low-frequency noise emissions of a WT with variable rotational speed and pitch. He uses a moderately turbulent inflow (turbulence intensity of 16%), which causes only a weak intervention of the controller and thus has little effect on the aerodynamic loads. He found that the amplitude of the sound pressure in this case remains almost unchanged by the controller, and the only effect is a slight shift of the frequencies in the sound spectrum.

## 1.2 | Low-frequency noise of wind turbines

A good overview of the noise emissions of wind turbines and the underlying mechanisms as well as approaches for calculation can be found in the book by Wagner et al.<sup>10</sup> The flow-induced noise mechanisms, called aeroacoustics, generate sound over a wide frequency range. The acoustic equations are derived from the more general flow equations, and the flow fields are the basis for aeroacoustic phenomena. For comprehensive information on, the general concepts and equations, please refer to literature (e.g., Delfs<sup>11</sup> or Sengupta and Bhumkar<sup>12</sup>). While the sources of acoustic emissions from wind turbines in the audible range have been extensively researched and various methods are used to reduce aerodynamic and mechanical noise,<sup>13</sup> much less is known about low-frequency sound emissions from wind turbines. Low-frequency noise has a smaller dissipation factor in air and can travel farther than high-frequency noise. This was found in measurements<sup>14,15</sup> on the infrasound propagation for distance up to 10 km, especially for stable atmospheric conditions. Hence, the extent to which such low-frequency emissions can be perceived by humans living in the vicinity of the WT is the subject of intensive research and is sometimes controversially discussed. This paper does not deal with this topic, but focuses on the mechanisms for the generation of low-frequency emissions from wind turbines.

The main noise mechanism on which the low-frequency sound emissions of WTs are based is the temporal change in the amplitude and direction of the force acting on the air from a surface.<sup>10</sup> The frequency of the load fluctuations corresponds to that of the emitted sound and the amplitude determines the sound power. Therefore, it is crucial for the evaluation of low-frequency aeroacoustics to take into account all features that influence the aerodynamics, which also includes the controller. Besides the dominant loading noise, the thickness noise due to the moving blades and fluctuating Reynolds stresses in the turbulent flow of the blade wake are sources of low-frequency acoustic emissions. Various aerodynamic phenomena cause load variations on WTs, including above all the blade-tower interaction (BTI), the interaction of the blades with inflow turbulence (IT) and the periodic vortex shedding (VS) at the tower in the form of a von Kármán vortex street. Hansen and Hansen<sup>16</sup> provide a

detailed literature review of the current state of research on noise emissions from WTs. Among other things, they conclude that better methods are needed to predict the effects of different topography and different meteorological conditions on the sound power levels of WTs. Only one study has been found that allows a prediction of the generation of infrasound based on atmospheric inflow parameters. In D'Amico et al,<sup>17</sup> a detailed long-term measurement campaign is presented that combines infrasound measurements in the vicinity of WTs with meteorological measurements to investigate the noise emitted by WTs as a function of meteorological parameters. A distinction was made between tonal BTI-noise and broadband IT-noise. An artificial neural network was used to derive physical relationships between the meteorological situation and the emitted low-frequency sound. With this, they found that mean wind speed, turbulence intensity and turbulent vertical heat flux are the most important factors for infrasound emission.

BTI as the main cause of low-frequency emissions from WTs has not only been investigated experimentally by measurements, as in the study mentioned above, but has also been proven by numerical simulations. The aeroacoustic emissions can only be predicted correctly if the underlying aerodynamics are captured with a high degree of accuracy. CFD simulations of fully resolved WTs represent the approach of highest quality. Based on Lighthill's acoustic analogy,<sup>18</sup> the Ffowcs Williams-Hawkings (FW-H) equation<sup>19</sup> allows to calculate the generation of sound from aerodynamic results by means of elementary sources, namely monopoles (moving volume), dipoles (forces acting onto the fluid) and quadrupoles (fluctuating Reynolds stresses). Yauwenas et al<sup>20</sup> and Klein et al<sup>21</sup> are among the few to realize this and also consider the entire surface of the WT, i.e. blades and tower, as a source of sound emissions. The first study focuses on BTI-noise, while the second study also considers IT-noise and VS-noise ( $f < 20$  Hz). In order to extend the frequency range with this numerical approach, the spatial and temporal resolution of the CFD simulation must be refined accordingly. This is computationally unfeasible for complex flow situations.<sup>22</sup> Therefore, semiempirical models for the noise sources based on flow parameters can be used to estimate the noise emissions, as presented in Cheng et al<sup>23</sup> in a state-of-the-art framework.

### 1.3 | Scope and objectives

The author's previous works<sup>22,24</sup> on low-frequency noise emissions from WTs deal with flow situations in complex terrain. They investigate the impact of turbulent wind fields with constant mean wind speed and direction and thus constant operating conditions on the surface pressure fluctuations and the resulting noise emissions, respectively. In Wenz et al,<sup>22</sup> among other things, the characteristics of the noise spectrum are analysed, with tonal peaks at the blade passing frequency (BPF) and its harmonics due to the BTI, which depend on the rotational speed, and the broadband level associated with the IT. Moreover, the directivity of the different noise sources (BTI, IT, VS) is presented in polar plots to analyse the underlying mechanisms. The aim of the simulation in this article is to extend these works and investigate the low-frequency noise emissions of a wind turbine under rapidly changing wind conditions (unsteady operating conditions). For this purpose, a aero-servo-elastic DDES of a fully resolved 2 MW wind turbine is conducted with the CFD solver *FLOWer*. A measured flow situation with strong changes in wind speed and direction is reproduced by using data from a precursor simulation with the meteorological code *PALM*, which was calibrated with lidar data, as inflow for *FLOWer*. The structural model in *SIMPACK* allows deformations of the tower as well as the blades and includes a controller that adjusts the rotational speed, the pitch angle and the yaw. The high-fidelity aerodynamic results are used to evaluate the low-frequency ( $f < 20$  Hz) noise emissions with the FW-H solver *ACCO* at multiple observer positions. On the one hand, the feasibility of the simulation is to be demonstrated and, on the other hand, aeroacoustically conspicuous operating points or influential flow parameters are to be identified.

## 2 | NUMERICAL TOOLS

The low-frequency aeroacoustic emissions from a generic 2-MW wind turbine are investigated numerically. The high-fidelity process chain for fluid-structure coupled CFD simulations under realistic turbulent inflow conditions comprises several solvers. Figure 1 shows schematically the connections of the process chain. The meteorological large eddy simulation (LES) solver *PALM* for simulating the meteorological situation provides the inflow conditions for an unsteady high-resolution delayed detached eddy simulation (DDES) of the WT near-field with the CFD solver *FLOWer*. The geometrically resolved WT is included in this simulation and a time-accurate coupling to the structural solver *SIMPACK* enables the consideration of aeroelastic effects caused by the fluid-structure interaction (FSI) as well as adjustments of the operational conditions by the use of a controller. The acoustic evaluation is done as post-processing with the Ffowcs Williams-Hawkings (FW-H) code *ACCO*. The *FLOWer-SIMPACK-ACCO* process chain was first presented in Klein et al,<sup>21</sup> where fundamental studies on BTI and the influence of aeroelasticity on low-frequency noise emissions can be found.

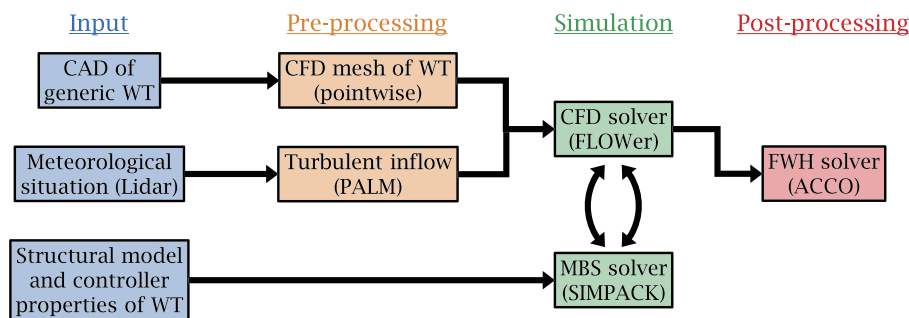


**FIGURE 1** Diagram of the numerical process chain.

## 2.1 | Meteorological CFD code—PALM

The parallelized LES Model *PALM* is a turbulence-resolving code developed at the Institute of Meteorology and Climatology (IMUK) of Leibniz University Hannover. The most recent description of the program can be found in Maronga et al.<sup>25</sup> It is based on the incompressible Navier-Stokes equations in Boussinesq-approximated form. It provides a LES mode and allows for external forcing and nesting to reproduce atmospheric flow situations.

## 2.2 | Unsteady CFD solver—FLOWer

The core of the numerical simulation of the WT is the CFD solver *FLOWer*, which was originally developed by the German Aerospace Center (DLR).<sup>26</sup> It is a compressible, block structured Reynolds-averaged Navier-Stokes (RANS) solver. The numerical scheme is based on a finite-volume formulation. The implemented *Chimera* overlapping mesh technique allows the use of independent grids for the individual components of the WT and the background. The solver has been continuously extended at the Institute of Aerodynamics and Gas Dynamics (IAG) of the University of Stuttgart to improve its suitability for wind turbine simulations. Among others, a fifth-order weighted essentially non-oscillatory scheme WENO is available for spatial discretization<sup>27</sup> and several hybrid RANS/LES schemes<sup>28</sup> have been implemented in *FLOWer*. Furthermore, a Dirichlet boundary condition is available to prescribe spatially and temporally varying atmospheric turbulence at the inflow,<sup>29</sup> for example stemming from precursor simulations. The work of Klein et al.<sup>21</sup> introduced a bidirectional coupling to the MBS simulation tool *SIMPACK*.

## 2.3 | Structural MBS solver—SIMPACK

*SIMPACK* is a commercial software for the simulation of multibody systems. The dynamic systems can consist of rigid and flexible bodies connected by joint elements. The flexible WT components such as the tower and blades can be modelled either as beams or as modal bodies by reading in the modal properties. External forces, such as aerodynamic forces, can be defined internally or imported from other programs via a predefined interface environment. Controllers can also be integrated. *SIMPACK* is frequently used by industrial and research groups for the simulation of WTs, for example, Luhmann et al.<sup>30</sup> and Guma et al.<sup>31</sup>

## 2.4 | Aeroacoustic FW-H solver—ACCO

The sound pressure  $p'$  is evaluated by means of the FW-H acoustic solver *ACCO*<sup>32</sup> using the surface pressure fluctuations on tower and blades from the coupled *FLOWer* simulation as in Wenz et al.<sup>22</sup> As described in the introduction, the FW-H equation considers three elementary sources, from which the quadrupoles are neglected when the WT surfaces are used as input. This is reasonable since the fluctuations in Reynolds stresses cause little noise at the low Mach numbers that occur at WTs, as shown by Ghasemian and Nejat.<sup>33</sup> Turbulence-induced noise is nevertheless captured, as the vortices interact with the WT surface and cause surface pressure fluctuations there.<sup>24</sup> Ground reflections and nonlinear propagation due to atmospheric stratification and turbulence are not captured. Hence, an undisturbed propagation and observers located in the acoustic far field are assumed. The contribution of mechanical noise is not considered. The highest captured frequency is limited by the CFD time step and mesh resolution to  $f < 20$  Hz.<sup>22</sup>

### 3 | COMPUTATIONAL SETUP

#### 3.1 | Studied wind turbine and situation

The studied generic 2.3-MW WT<sup>34</sup> has a rotor diameter of 82 m and a hub height of 97 m and is named I82. The rated rotational speed is  $n_{rated} = 18$  rpm at a wind speed of  $14 \text{ ms}^{-1}$ . The generic I82 is aero-servo-elastically similar to the commercial E82. To ensure that a realistic event is simulated, a situation measured by Wobben Research and Development GmbH (WRD) at the Harsewinkel site in Northern Germany is reproduced. The situation is chosen based on operational data from the commercial WT in Harsewinkel and lidar measurements close by. A 5-min interval on 22/08/2020 from 16:42:20 to 16:47:20 is selected, during which a strong rotation as well as acceleration of the wind occurred. All controllers of the commercial WT show reactions in this time window and especially the yaw controller struggles to compensate the wind direction change fast enough, which makes the situation an extreme event for the WT and interesting to be numerically studied. In Figure 2, a section of the wind speed and direction at hub height measured by a lidar 245 m beside the WT is shown. The area marked in green represents the simulated time period that will be evaluated in the following, while the section marked in yellow served to initialize the simulation. During the evaluation period, the wind turns from southwest by about  $60^\circ$  towards northwest and the wind speed increases by  $5 \text{ ms}^{-1}$ . The mean levels are each overlaid by short-time fluctuations. The meteorological cause behind the observed extreme event was a cold front passage and thus represents a regularly occurring event.

#### 3.2 | Meteorological precursor simulation with PALM

A LES with the meteorological model system *PALM* provides the spatially and temporally resolved wind field of the situation. To replicate the meteorological conditions at the site, *PALM* could be driven with a larger scale weather model that contains the cold front passage. However, due to the coarse spatial and temporal resolution of these models, the fast changes in wind speed and direction observed at the site cannot be reproduced. Thus, the so-called *nudging* approach according to Anthes<sup>35</sup> is applied. The nudging adjusts the horizontally averaged velocity profiles towards the (temporally changing) measured velocity profiles by adding an additional tendency on every grid point. The adjustment speed is steered by the nudging time scale, which is usually set to the order of several hours so that the flow can follow the slow changes in the synoptic-scale flow.<sup>36</sup> In this case, however, the time scale is set to 10 s so that the rapid changes in wind speed and wind direction can be reproduced.

The *PALM* computational domain is 7.2 km long, 3.6 km wide and 3.0 km high, and cyclic boundary conditions are applied. It has a grid width of 2 m and is calculated with a time step of 0.05 s. Forest areas as well as ground roughness are taken into account. A convective boundary layer driven by a ground sensible heat flux of  $0.2 \text{ Kms}^{-1}$  and a height of 1000 m is simulated. To obtain realistic initial wind and temperature profiles, a pre-run with a grid spacing of 20 m and a simulated time of 15 h is performed. The *PALM* calculation is a purely meteorological simulation, representing the empty terrain without the WT.

For the transfer to *FLOWer* an interface between *PALM* and *FLOWer* is used, which was developed within the AssiSt project.<sup>37</sup> The unsteady *PALM* result is extracted in a vertical  $y$ - $z$  surface at the position of the WT, which is 5.8 km away from the *PALM* inflow boundary. This wind field is processed and injected at the *FLOWer* inflow via the Dirichlet boundary condition implemented by Meister.<sup>29</sup> Thereby, the temporally and spatially coarser resolved *PALM* result is linearly interpolated to the *FLOWer* grid points and time steps. The *nudging* forces in the area 6R in front of the WT are essential in *PALM* for the developments of the wind field. Since these are not considered in *FLOWer*, an extraction of the wind field from the *PALM* calculation at the position of the *FLOWer* inflow plane for use as input in *FLOWer* is not possible. Due to the propagation distance from the inflow boundary to the WT position in *FLOWer*, there is a time offset between the *PALM* and *FLOWer* flow results at the WT position.

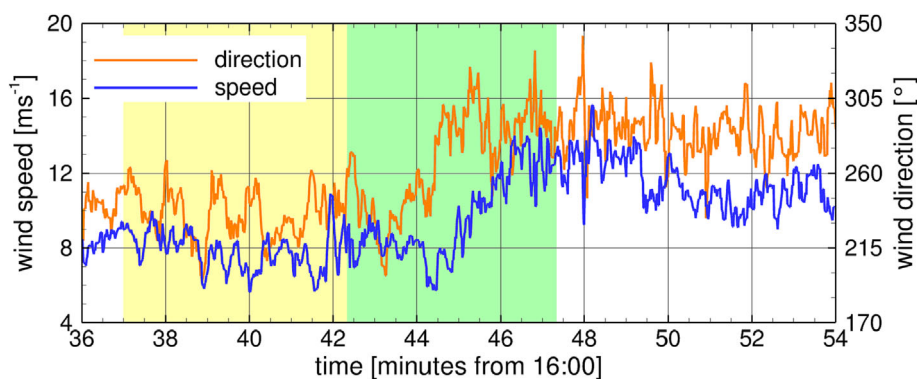


**FIGURE 2** Section of the wind speed and direction curve at hub height, measured by a Lidar system at the Harsewinkel site.

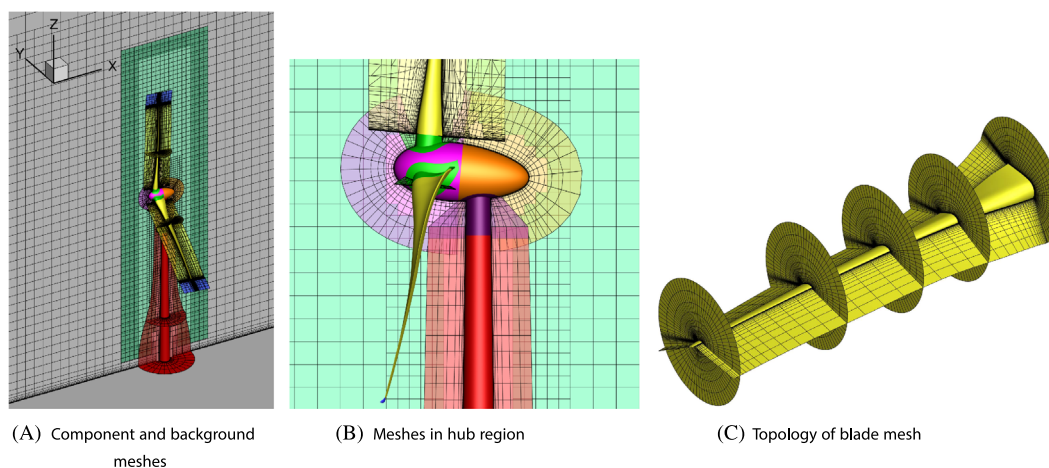


**FIGURE 3** Assembly of the CFD model. Only every fourth grid line is shown.

### 3.3 | CFD model in FLOWer

The computational setup of the generic WT is taken from Wenz et al.<sup>24</sup> The CFD model of the I82 wind turbine for the simulation with *FLOWer* consists of 17 independent meshes, which are embedded in a background mesh with a flat ground, and are connected with the *Chimera* overlapping mesh technique, as shown in Figure 3. The boundary layer of all WT components is fully resolved ( $y^+ < 1$ ) and the blades are meshed in an O-topology. The inflow boundary is placed as close as possible to the WT ( $\Delta x = 6R$ ),<sup>38</sup> in order to keep the necessary lateral expansion of the finely meshed area in the inflow of the WT within reasonable limits in case of strong wind rotation. The CFD computational domain is oriented so that the x-axis is parallel to the wind direction from 260°, resulting in similar maximal yawed inflow from positive and negative y-directions. The background mesh has a flat bottom, a 1 m resolution in the area of interest and consists of 91.2 million cells including refinement (green in Figure 3A) and bottom boundary layer. No vegetation is considered. The second-order Jameson-Schmidt-Turkel (JST) scheme is used for spatial discretization in the component meshes whereas the fifth-order WENO scheme is applied in the background mesh. The unsteady simulation with *FLOWer* is carried out as DDES<sup>39</sup> based on the Menter SST  $k - \omega$  RANS model.<sup>40</sup> The flow is considered to be fully turbulent. An implicit second-order dual time-stepping scheme is deployed for time integration. A physical time step  $\Delta t = 0.01$  s (corresponding to less than 1° azimuth at rated conditions) with 80 inner iterations is applied for the evaluated part of the simulation.

### 3.4 | Structural model in SIMPACK

The structural model of the generic I82 in *SIMPACK* was created by Arnold et al.<sup>34</sup> Each rotor blade consists of 29 flexible, nonlinear beam elements (Timoshenko) that are rigidly connected to each other. The Rayleigh model is used for the damping of the rotor blade structure. The advantages of modelling a rotor blade as MBS have been presented in detail by Matha et al.<sup>41</sup> This method provides a geometric nonlinear blade model, which as Gözcü and Verelst<sup>6</sup> show, leads to significantly smaller and more realistic deformations than linear blade models. It also captures the bending-torsion coupling. The radial distribution of the mass, the moments of inertia, the bending, torsional and tensile stiffness as well as the position of the centre of gravity, the shear centre and the stiffness axis are specified. The tower is also represented as MBS, and consists of 97 flexible, linear beam elements (Euler–Bernoulli). The material properties are chosen to match a hybrid steel-concrete tower. Hub, nacelle, drive train and foundation are defined as rigid bodies. The centrifugal force induced by the blade rotation and the gravitational force are considered in *SIMPACK*. An integrator with variable step size is used to calculate the deformations to ensure that all model states are kept within predefined tolerances at each time step. All eigenfrequencies below 15 Hz are considered in *SIMPACK*.

The generic controller is also implemented in *SIMPACK*. The control concept is based on that of the three reference wind turbines NREL 5 MW,<sup>3</sup> IWES IWT-7.5-164<sup>4</sup> and DTU 10 MW<sup>5</sup> and was combined by Arnold et al.<sup>34</sup> The point of operation results from a power control in the generator, a speed control via the pitch angle  $\gamma$  and a yaw control. The rotational speed in the partial load range is controlled via the power control. It is based on the optimal operating point of the generic WT at a tip-speed ratio  $\lambda_{opt} = 7.5$  and a power coefficient  $c_{P,opt} = 0.5$ . The pitch control ( $\dot{\gamma} = 5^\circ \text{ s}^{-1}$ ) serves on the one hand to control the power and thus the rotational speed, and on the other hand to reduce peak loads (*peak*

\*The minimum width  $\Delta y$  of the area to be finely meshed is given by  $\Delta y = \pm(\tan(\Delta\Phi_{max}/2) \cdot \Delta x + R)$  with  $\Delta x$  being the distance from the inflow boundary to the WT and  $\Delta\Phi_{max}$  the maximum wind direction change.

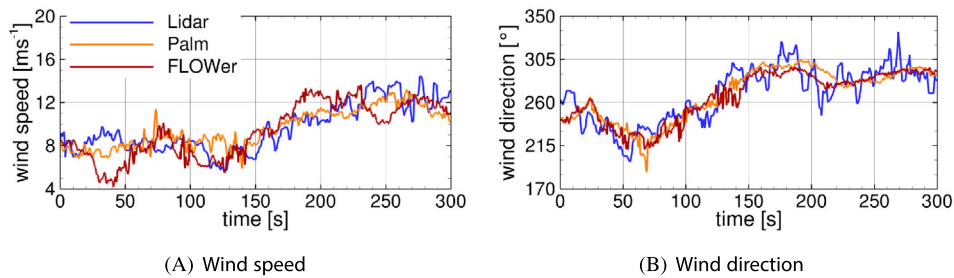


**FIGURE 4** Wind speed and direction at hub height at the WT position, measured by the lidar system, simulated with PALM and with FLOWer (empty box simulation).

shaving) in the upper partial load range, in the event of storms or strong yawed inflow. In addition to the current power, the wind situation at the anemometer also influences the control. Since the anemometer is located close behind the rotor, the measured<sup>†</sup> anemometer wind speeds (parallel and transverse to the nacelle) must be corrected for the rotor blockage and the counter-rotating swirl in the wake of the rotor. For this purpose, correction curves calibrated to the I82 are used for speed and direction.<sup>34</sup> Further information on this can be found in Appendix A. In addition, a low-pass filter is applied to smooth the signal. Based on the corrected anemometer wind direction, the yaw controller causes a repositioning of the nacelle ( $\dot{\Phi} = 0.4^\circ \text{ s}^{-1}$ ) in case of large or continuous misalignment  $\Delta\Phi$ . An adjustment does not take place continuously, but cyclically after a limit value is exceeded. In order to use this control strategy of the I82 in the simulation, the anemometer wind speeds are transferred from FLOWer to SIMPACK in addition to the loads.

### 3.5 | Fluid-structure coupling

An explicit coupling scheme is applied between SIMPACK and FLOWer with both solvers running in a sequential way (partitioned approach). Thus, the resolutions of the CFD and MBS models are independent of each other. In this process, SIMPACK runs ahead and uses the CFD loads of the previous time step to calculate the deformations and controller reactions. After each physical time step, information is exchanged by means of files. They contain displacements (translation and rotation) or aerodynamic loads (forces and moments) at a total of 110 discrete positions, so-called markers, of which 29 markers are assigned to each blade, 21 markers to the tower, and one marker each to the nacelle and hub. The anemometer velocities are appended to the file with the loads and the controller changes are included in the communicated deformations. The surface mesh is reduced to a point cloud that deforms according to the markers. A cubic spline interpolation is applied for the mapping of the flexible structures (beams). The cells of the volume mesh are linked to the point cloud via radial basis functions and thus also deform accordingly. Further details can be found in Klein et al<sup>21</sup> and a validation of the FLOWer-SIMPACK coupling with an elastic cantilever beam in Klein.<sup>9</sup>

## 4 | RESULTS

### 4.1 | Flow field in the vicinity of the turbine

In the following, the flow situation resulting from FLOWer at the WT position is briefly explained. The results are from an additional simulation without WT, where the inflow data extracted from PALM was propagated through the empty background mesh. Figure 4 shows the simulated wind speed and direction at hub height at the WT position compared to the measured conditions and the PALM result. The time  $t$  for the evaluation of the simulation is from now on always given in seconds, starting from 16:42:20. It can be seen that the measured situation is reproduced in PALM and the trend is preserved in FLOWer from the inflow boundary to the WT position. For the wind speed in Figure 4A, a stronger decrease is seen in FLOWer between  $t = 25$  s and 50 s, and in Figure 4B, it can be seen that already in PALM the fluctuations of the wind direction are damped. The deviation is attributed to too low a ground sensible heat flux in PALM, so that an excessively stable atmospheric boundary layer and thus too low a turbulence intensity was simulated. However, the characteristic of a fast and strongly rotating wind direction in combination with an acceleration of the wind is clearly reproduced with the simulation chain.

Figure 5 shows the temporal development of the vertical wind shear at the WT position. The increase of the horizontal wind speed  $u_h$  with height changes significantly over time. Particularly relevant for the behaviour of the WT is the area of the rotor disc, where slight shear is only

<sup>†</sup>In the numerical simulation, 'measured' means extracted from the volume flow solution.

visible around the marked time points 2 and 4. Especially during the last 100 s of the evaluation period the speed is almost homogeneous over the rotor plane. The vertical wind shear can therefore be neglected in the analysis of the results.

The turbulence intensity  $TI$  is commonly determined from 10-min intervals in meteorology and for the design of WTs. However, this requires a stationary wind situation during the interval. If this is not the case and there is a trend, i.e. a slow change in the mean wind speed, this must be compensated for before determining  $TI$ .<sup>42</sup> In the simulated flow situation, the change in flow occurs on significantly smaller time scales, which is why  $TI$  is determined here from 30-s intervals. In addition, the trend of the wind speed in each interval is compensated before calculating the standard deviation. The trend is defined, following Hart et al.<sup>43</sup> and Larsen and Hansen,<sup>44</sup> as the sum of all Fourier modes of the wind speed time series whose period is longer than the evaluation interval. The cut-off frequency of the high-pass filter is hence  $f_c = 1/30$  Hz. Figure 6 shows the height-dependent evolution of  $TI_{30s}$  over time. Around the marked time points 2 and 4, stronger turbulence occurs in the lower half of the rotor disc. Otherwise  $TI$  is relatively constant over the rotor and clearly below 10%.

## 4.2 | Aero-servo-elastic analysis of the turbine

First, the aero-servo-elastic simulation is evaluated. It should be noted that the aerodynamics, the structural dynamics and the control of the WT are closely interlinked and influence or condition each other. Therefore, a separate evaluation of the corresponding variables is not recommended. In Figure 7, the essential control variables, the power and the thrust as parameters for the aerodynamic performance, and the deformation of the blades and the tower are shown over the simulated meteorological situation. The time  $t$  runs in seconds from 16:42:20 so that the result of the simulation after the initialization of the flow field, the deformation and the controller is displayed. The rotational speed  $n$  in Figure 7A correlates, as expected, for the most part with the wind speed (see Figure 5). Only in the time range from about 180 to 245 s  $n$  is clearly reduced. The reason for this can be seen in Figure 7B. From 160 s, the nacelle is compensating the wind direction change (compare Figure 4B) with maximum yawing speed but is not fast enough, so that the nacelle misalignment  $\Delta\phi$  keeps increasing. Therefore, from 180 s, a load reduction mode of the controller takes action to protect the WT due to too strong yawed inflow. The plotted nacelle misalignment  $\Delta\phi$  is the value the controller extracts from the anemometer data. As described in Section 3.4, the anemometer velocities are corrected with calibrated correction factors. In Appendix A, it can

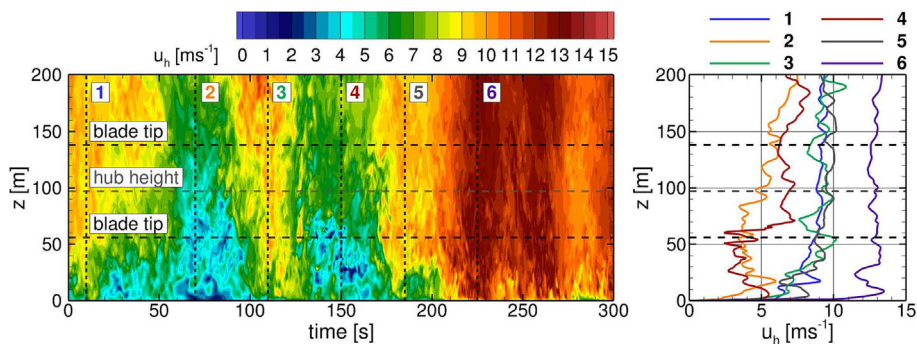


**FIGURE 5** Horizontal velocity  $u_h$  at the WT position over time and height  $z$  simulated with *FLOWer*, and vertical velocity profiles at discrete points in time (empty box simulation).

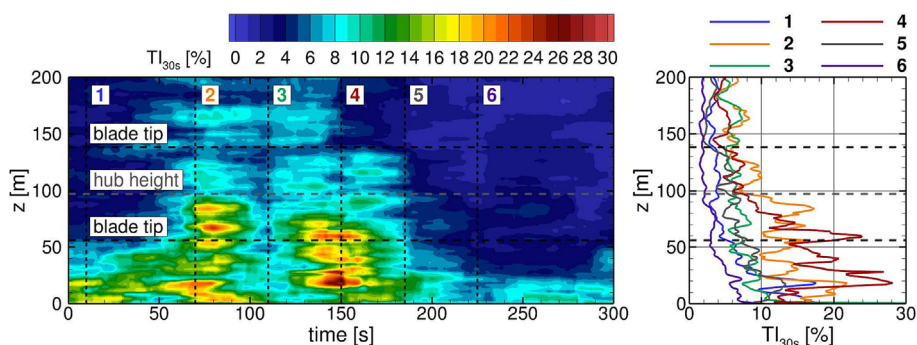


**FIGURE 6** Turbulence intensity  $TI_{30s}$  simulated with *FLOWer* (trend-adjusted, from 30-s intervals) at the WT position over time and height  $z$ , and vertical turbulence intensity profiles at discrete time points (empty box simulation).



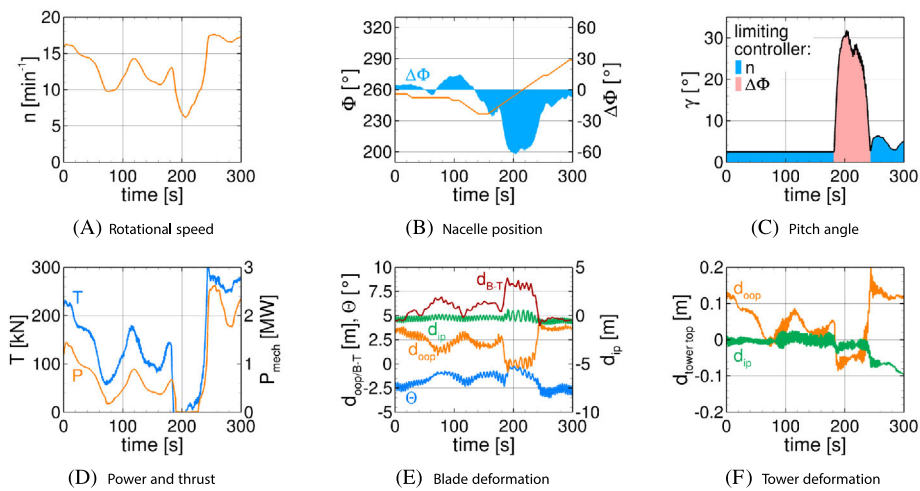


**FIGURE 7** Development of the rotational speed  $n$ , the nacelle position  $\phi$ , the nacelle misalignment  $\Delta\phi$ , the pitch angle  $\gamma$ , the aerodynamic thrust  $T$ , the mechanical power  $P_{mech}$ , the blade tip bending  $d_{oop,ip}$  and torsion  $\theta$ , the clearance between blade tip and tower  $d_{B-T}$  as well as the tower top deflection  $d_{oop,ip}$ .

be seen that these are not optimally calibrated for the generic I82 and especially in load reduction mode lead to an overestimation of the oblique flow of about  $20^\circ$ . The wind direction at 200 s is about  $295^\circ$ , as can be seen in Figure 4B, while the nacelle position is at  $\phi = 255^\circ$ , giving a nacelle misalignment of  $40^\circ$ , which the controller incorrectly estimates to be  $60^\circ$ . As a result, the pitch angle  $\gamma$  seen in Figure 7C is increased somewhat too much. However, the basic pitch behaviour is correct. The pitch change significantly reduces the aerodynamic torque and, following the points of operation, also the rotational speed. Correspondingly, the mechanical power  $P_{mech}$  generated by the WT drops to zero in this time range, as shown in Figure 7D. The load reduction period is followed by operation of the WT at almost full load as soon as the yaw controller has aligned the nacelle with the wind direction again. This manifests itself in a relatively constant rotational speed close to  $n_{rated}$  as well as a high power generation. The thrust  $T$  is also very strong in this time range, but fluctuates less than the power. The simulated meteorological event can thus be divided into three time periods with different operating modes. From 0 to 180 s, the WT operates in the lower partial load range at low inclined flow and is controlled by the power controller. From 180 to 245 s, there is a strong inclined flow and the pitch and yaw controllers control the WT in load reduction mode to protect against overload. This is followed by an operation of the WT at almost full load from 245 to 300 s in which the rotational speed controller controls the pitch angle in order not to exceed  $n_{rated}$ .

Each point of operation resulting from the control and the inflow generates a characteristic aerodynamic load in interaction with the blade geometry of the I82. This, together with the influences of the mass<sup>‡</sup> and the structural properties, drives the deformation of the WT. In Figure 7E, the deformation of the blade tip is shown (index B). The out-of-plane motion  $d_{oop,B}$  correlates in its course with the thrust, as expected, but is superimposed by small fluctuations per revolution. The fluctuations are strongest around 200 s, when the aerodynamic loads are zero. This indicates that during power production, the aerodynamic damping mitigates the flapping oscillations. Of course, an unequal distribution of flow velocity (e.g. vertical wind shear) or turbulence over the rotor disc also have a direct impact on the periodic vibrations. For the in-plane deflection  $d_{ip,B}$  the influence of the aerodynamic loads on the damping of the revolution-coupled oscillations can be observed even more clearly. Apart from that, it can be seen that the deflection in-plane is significantly smaller than out-of-plane and the gravity-induced periodic fluctuations dominate over the influence of the aerodynamic loads. The blade tip torsion  $\theta$  also follows the thrust (reversed sign) and there is a reduction in the effective angle of attack due to the torsion of the blade with increasing loads on the blades. For the acoustics investigated in the following section, the flapping motion is particularly relevant, as it changes the blade-tower distance. The resulting clearance between blade tip and tower  $d_{B-T}$  at each passage is also plotted. The movement of the tower top (index T) in Figure 7F is relatively small. The flapping motion  $d_{oop,T}$  again follows the aerodynamic thrust and is superimposed by small fluctuations. When no power is generated, the weight of the rotor causes the tower to bend in the direction of the inflow. The in-plane motion of the tower top  $d_{ip,T}$  contains larger fluctuations due to the reduced aerodynamic damping in this direction. Under full load, there is a significant deflection in the negative  $y$  direction. This matches the torque transferred from the rotor to the tower top.

From the analysis of the operating parameters, the performance and the blade tip and tower top deformations, it can be seen that the numerical process chain realistically simulates the operation of the WT during the controller demanding situation. This lays the foundation for the aeroacoustic evaluation of the low-frequency emissions in the following section.

<sup>‡</sup>The mass distribution in the WT generates additional load inputs due to gravity and inertia.

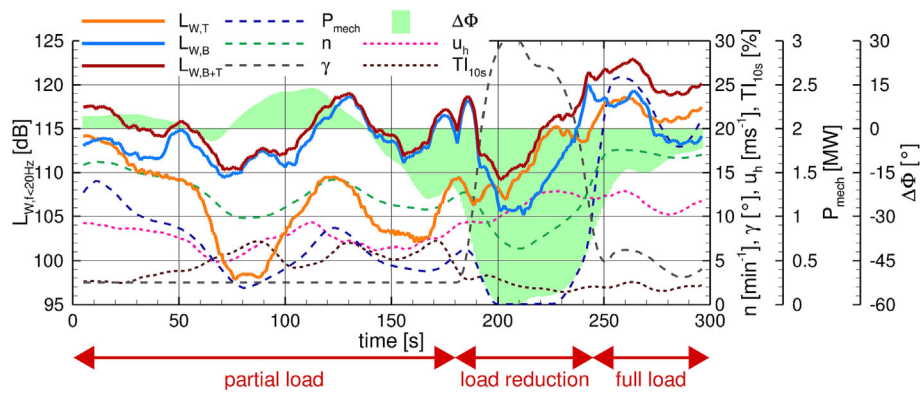


**FIGURE 8** Sound power level  $L_{W,f < 20\text{Hz}}$  from sliding 10-s intervals emitted by tower, blades and together. In addition, the 10-s mean values of the mechanical power  $P_{mech}$ , the rotational speed  $n$ , the pitch angle  $\gamma$ , the nacelle misalignment  $\Delta\Phi$ , the wind speed  $u_h$  and the turbulence intensity  $TI_{10s}$  are depicted.

### 4.3 | Acoustic analysis of the wind turbine

#### 4.3.1 | Sound power level

The strongly unsteady wind conditions and the resulting volatile operating behaviour make an acoustic evaluation averaged over the entire period of time not very meaningful. Therefore, the time evolution of the sound power level  $L_{W,f < 20\text{Hz}}$  as the global emission variable for low-frequency noise, is analysed over the simulation period. For this purpose, the sound pressure time series  $p'(t)$  is evaluated with ACCO at observer points distributed on a sphere, as described in Wenz et al.<sup>22</sup> Here, the effective sound pressure level  $L_p$  at each observer, which is necessary to calculate  $L_W$  is not calculated from the entire time signal, but only from 10-s intervals that are shifted through the time series<sup>8</sup> in 1-s steps. In Figure 8, the course of the low-frequency sound power levels emitted by the tower  $L_{W,T}$ , the blades  $L_{W,B}$  and together  $L_{W,B+T}$  is shown. In order to be able to relate the anomalies more easily to the operating conditions at the same time, the mean values of the respective interval of the mechanical power  $P_{mech}$  the rotational speed  $n$  the nacelle misalignment  $\Delta\Phi$  and the pitch angle  $\gamma$  are also shown. In addition, the curves of the wind speed  $u_h$ <sup>4</sup> and the turbulence intensity  $TI_{10s}$  are shown.  $TI_{10s}$  represents the value from sliding, trend-adjusted 10-s intervals, averaged over the vertical rotor extension. The underlying wind speed time series were extracted one rotor radius ahead of the WT and corrected for propagation time to the rotor plane.<sup>#</sup>

It is noticeable that the total emission  $L_{W,B+T}$  follows the course of the rotational speed or power fairly well. The sound emission of the tower is clearly more sensitive to changes and fluctuates more strongly. It can also be seen that the blades are the stronger emitters in the lower partial load range. However, as soon as the blades are strongly pitched due to the yawed inflow, the emission of the blades is reduced while the sound power emitted by the tower increases. At approximately 77, 194 and 234 s, the rotational speed and mechanical power are almost identical with  $n = 10\text{rpm}$  and  $P_{mech} = 0.2\text{MW}$ . At the first of these points in time, the WT is in partial load operation, while at the other two, the pitch angle is increased to  $23^\circ$  to protect the WT and the nacelle misalignment is approximately  $50^\circ$ . From the first to the second instant of time, the low-frequency sound power level of the tower is increased by almost 10 dB while that of the blades is almost the same. At the third point in time, the emission of the tower increases by another 6 dB while the blade emissions increase by 3 dB. The differences between the second and third instant in time show that not only the operating point, which is identical, is decisive for the sound emissions, but that the flow situation also has an influence. The wind speed for example, increases from the second to the third point in time by  $3\text{ms}^{-1}$ . Even though the emissions of the blades also correlate strongly with the rotational speed, additional increases in the emitted low-frequency sound power can be observed at the moments 89 s and 174 s. This matches a short-term increase in turbulence intensity in each case. A direct correlation of the low-frequency sound emissions to slight nacelle misalignments which do not cause a pitch reaction, as they occur in the first 180 s, is not evident.

In order to better identify the dependence of the emitted low-frequency sound power level  $L_{W,f < 20\text{Hz}}$  on the operating and flow parameters, the value pairs are shown as scatter plots in Figures 9 and 10. The emitters are separated for the evaluation. In addition, the operating modes to which the value pair is to be assigned (compare Figure 8) are distinguished by symbols, partial load (diamond), load reduction (triangle) and full load (square). In the Figure 9A,B, the dependency of the emitted low-frequency sound power level on the rotational speed and the power of the WT,

<sup>8</sup>The noise generated at the WT at one point in time reaches the observer approximately 3 s later due to sound propagation over 1000 m. This was compensated accordingly in the time series.

<sup>4</sup>The wind speed from the simulation without WT is used instead of the anemometer value corrected by the controller because there is an offset as shown in Appendix A.

<sup>#</sup>Each point in time was shifted according to the current wind speed following  $\Delta t = \Delta x / u_h$ . A further deceleration of the flow velocity due to the induction of the rotor was neglected.

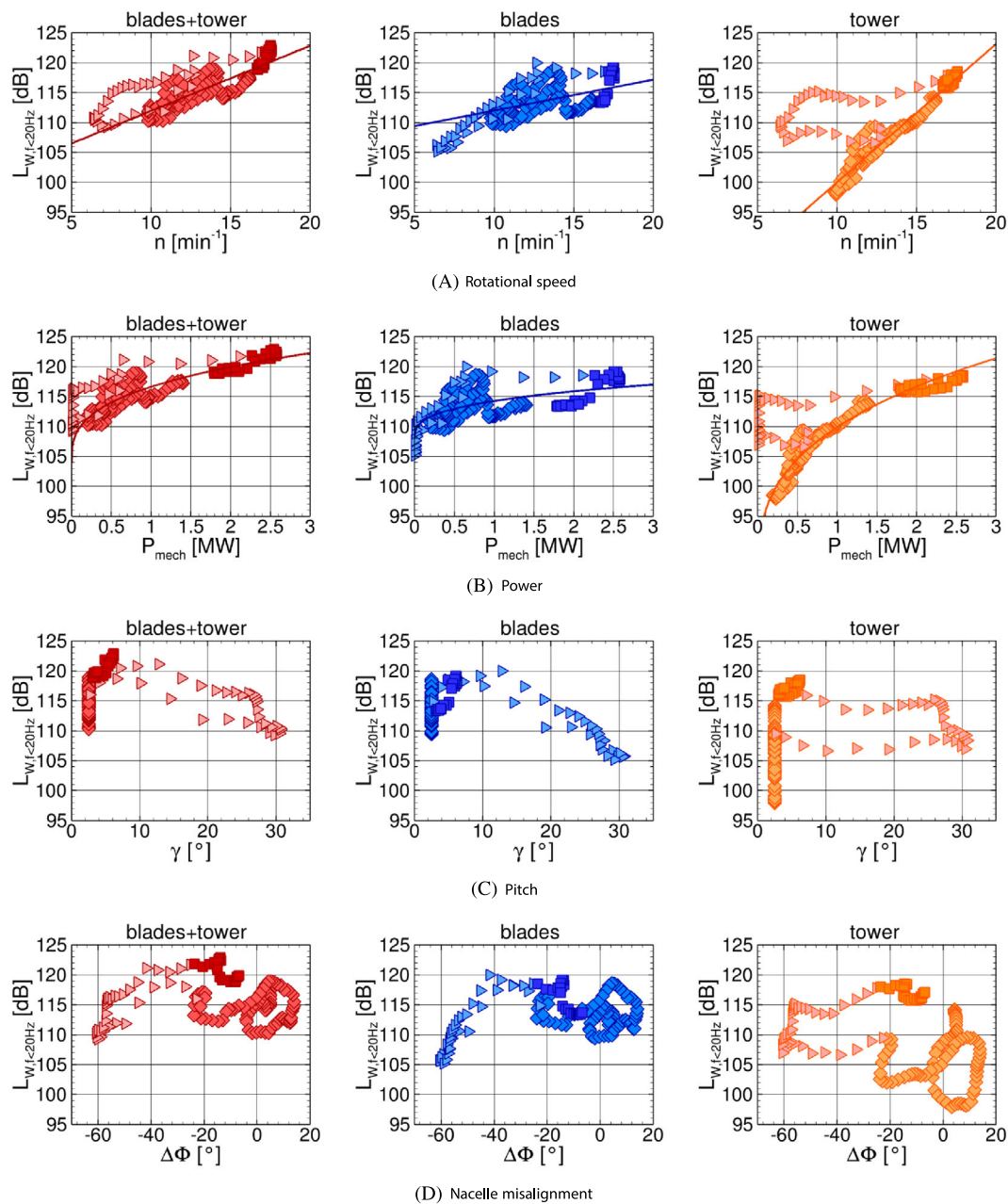


**FIGURE 9** Dependence of the sound power level  $L_{W,f < 20\text{Hz}}$  emitted by the tower, blades and together on the operating parameters, taking into account the operating mode (partial load  $\diamond$ , load reduction  $\triangleright$ , full load  $\square$ ). Shown are rotational speed  $n$ , mechanical power  $P_{\text{mech}}$ , pitch angle  $\gamma$  and nacelle misalignment  $\Delta\Phi$ .

which has already been noticed in Figure 8, becomes apparent in normal operation (partial load and full load). Trend lines<sup>||</sup> determined with the method of least squares are added. A linear regression is used to describe the relationship between  $L_{W,f < 20\text{Hz}}$  and the rotational speed, and for the dependence between  $L_{W,f < 20\text{Hz}}$  and the power,  $L_W(P) = a \cdot P^{1/3} + b$  is assumed as a model function with the regression coefficients  $a$  and  $b$ . This is based on the assumption that according to the control law  $n \propto u_{h,\infty}$  and that in general for the wind power  $P \propto u_{h,\infty}^3$ . Especially the sound emission of the tower follows the resulting trend lines very well, with determination coefficients  $R^2 > 0.95$ . If the low-frequency emissions of the blades are analysed, a somewhat larger scattering and consequently a less clear correlation becomes apparent ( $R^2 \approx 0.3$ ). Nevertheless, the slope of the trend line is clearly smaller, which shows that the low-frequency sound power emitted by the blades is less sensitive to the rotational speed than that emitted by the tower. The trend lines of the total emission of the WT lie between those of the blades and the tower with  $R^2 \approx 0.75$ . Since the regression analysis for  $n$  and  $P$  yields very similar  $R^2$  in each case, the proportionality assumptions made are valid for normal operation. For the

<sup>||</sup>The operating points in load reduction mode were neglected for the determination of the regression.

load reduction mode, the emissions deviate strongly from the observed trends and no clear correlation between the quantities is discernible. The wind speed  $u_h$  in Figure 10A, reveals a similar relationship, which is expected due to  $n \propto u_{h,\infty}$  during normal operation mode. In the load reduction mode, the low-frequency emissions are as expected lower for the same inflow velocities. The controller links  $n$  and  $\gamma$  to  $u_h$  and  $P_{mech}$  results, defining a strong dependence between these parameters. Hence, their correlation with the sound power shows similar trends. The pitch angle varies mainly in load reduction mode, showing a decrease in low-frequency sound power with increasing angle, as seen in Figure 9C. However, the pitch angle and the rotational speed are also directly linked and thus this trend cannot be clearly attributed to the pitch angle change. The Figures 9D and 10B do not show a clear dependence of the emitted low-frequency sound power level on nacelle misalignment or turbulence intensity.

As shown,  $L_{W,f < 20\text{Hz}}$  is directly dependent on the rotational speed, the power and the wind speed, which are linked to each other via the points of operation defined by the controller. However, especially the stronger dispersion for the blades indicates that the other parameters also have a direct influence on the emitted low-frequency sound power. Therefore, the influence of  $u_h$ ,  $\Delta\Phi$  and  $TI$  on  $L_{W,f < 20\text{Hz}}$  is investigated under consideration of the rotational speed. For this purpose, the scatter diagrams in Figure 11 are extended by one dimension, by displaying  $L_{W,f < 20\text{Hz}}$  via a colour scale. In Figure 11A, the linear correlation between  $n$  and  $u_h$  is confirmed in partial load operation, while an uncorrelated second branch is present for load reduction mode.  $u_h$  is thus an independent parameter in the load reduction mode. The emissions of the tower show a clear dependency of  $L_{W,f < 20\text{Hz}}$  to  $n$  in partial load operation and of  $L_{W,f < 20\text{Hz}}$  to  $u_h$  in load reduction operation. In the latter, emissions are higher than in the former at the same rotational speed and wind speed, respectively. The BTI is reduced in load reduction mode due to the lower aerodynamic forces on the blades. The higher low-frequency noise emissions can therefore be attributed to a stronger VS and dominant von Kármán vortex street at the tower, as it is less disturbed by the blade passage. Overall, the low-frequency sound emissions of the blades are less directly related to  $u_h$  and  $n$ . This can be seen from higher sound emissions at reduced  $n$  and  $u_h$  indicating an impact of a further parameter. In normal operation, Figure 11C shows that the emitted low-frequency sound power of the tower does not depend on  $\Delta\Phi$  and there is no clear trend in the emissions of the blades. In Figure 11D, a tendency of higher low-frequency sound emission at higher turbulence intensity can be observed for the blades in normal operation at the same rotational speed, while  $L_{W,f < 20\text{Hz}}$  from the tower is independent of  $TI$ .

It has been shown that the emitted low-frequency sound power of the tower depends on the rotational speed and on the wind speed, while the emissions of the blades are additionally influenced by the turbulence intensity. These numerical results match the findings from free-field measurements by Blumendeller et al,<sup>15</sup> who observed the same correlation between rotational speed and low-frequency sound emission, and by D'Amico et al,<sup>17</sup> who identified wind speed as well as turbulence intensity as dominant influencing factors. A yawed inflow is negligible for the sound emissions as long as it is not so large that the operating mode changes.

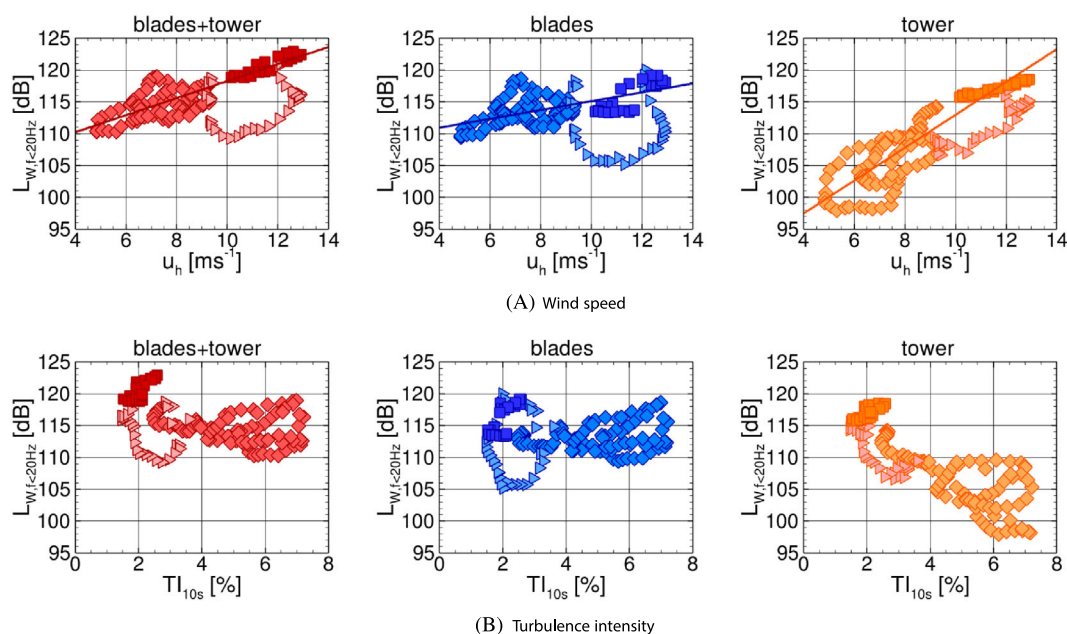


**FIGURE 10** Dependence of the sound power level  $L_{W,f < 20\text{Hz}}$  emitted by the tower, blades and together on the flow parameters, taking into account the operating mode (partial load  $\diamond$ , load reduction  $\blacktriangleright$ , full load  $\square$ ). Shown are wind speed  $u_h$  and turbulence intensity  $TI_{10s}$ .

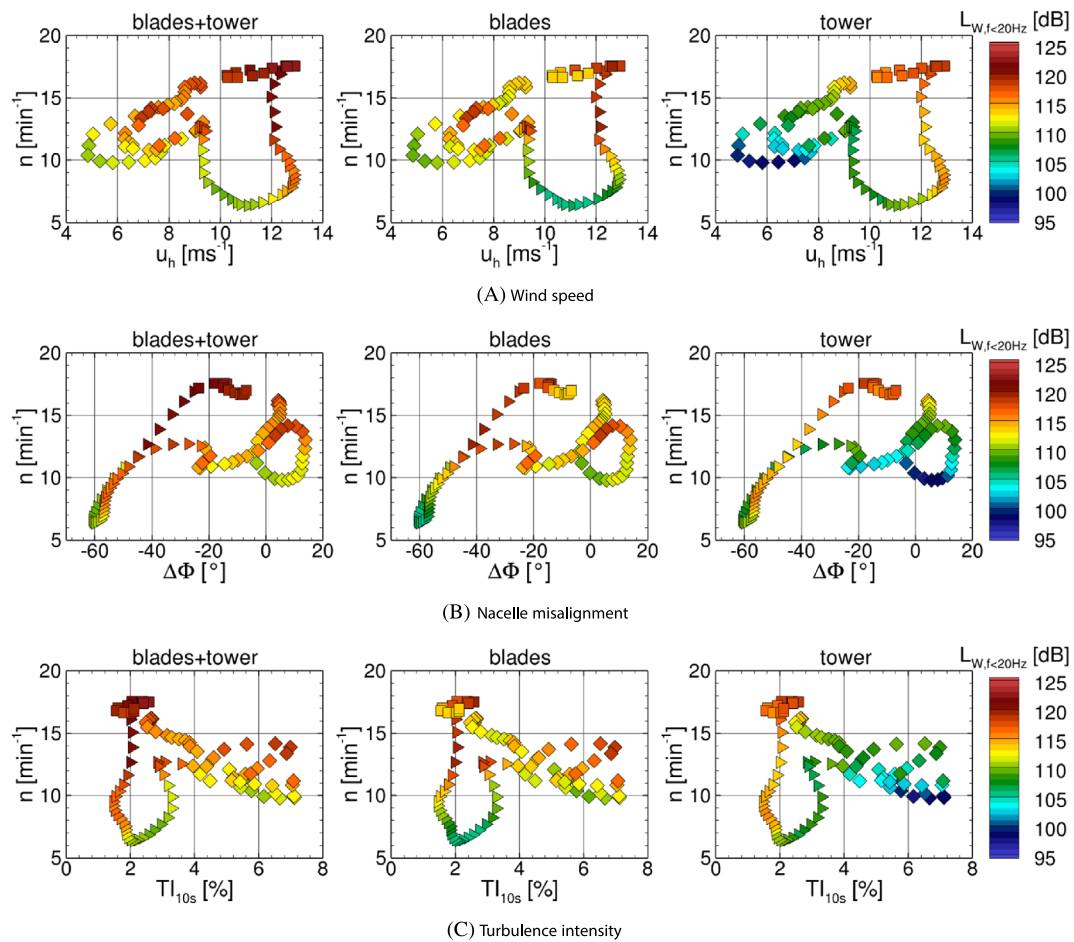


**FIGURE 11** Dependence of the sound power level  $L_{W,f < 20\text{Hz}}$  emitted by the tower, blades and together on the rotational speed  $n$  and another operating or flow parameter, taking into account the operating mode (partial load  $\diamond$ , load reduction  $\triangleright$ , full load  $\square$ ). Shown are the wind speed  $u_h$ , the nacelle misalignment  $\Delta\Phi$  and turbulence intensity  $TI_{10s}$ .

### 4.3.2 | Directivity of noise emissions

To further investigate the emission characteristics and directivity, the sound pressure levels  $L_p$  at 180 equiangular observer positions on a circle with 1000 m radius around the WT on the ground are analysed. This approach has already been used in Wenz et al.<sup>22</sup> where the directivity of the low-frequency noise mechanisms is depicted in polar diagrams. This illustration is well suited for cases with constant mean wind speed and direction. However, due to the yawing of the WT and the resulting relative motion of the directivity pattern to the fixed observers on a circle around the WT, the directivity pattern is distorted. Therefore, a different evaluation approach is chosen to analyse the directivity as well as the dominant frequency as a function of time. Since not only the low-frequency root-mean-square sound pressure level is of interest but also the loudest frequency and its peak level are relevant, a short-time Fourier transform (STFT) is applied, where 20-s intervals, which are shifted through the time series in 1-s steps, are used separately for the frequency analysis. This results in many consecutive narrowband spectra for each observer position with a frequency resolution of  $\Delta f = 0.05$  Hz. In Figure 12, the highest peak sound pressure level  $L_{p,max}$  of each generated narrowband spectrum is shown. That means for each time interval, there are 180 values (one for each observer position). Additionally, for the highest peak sound pressure level per time interval, the position of the corresponding observer point  $\Phi_{L_{p,max}}$  and the frequency  $f_{L_{p,max}}$  are shown. For reference, the BPF and three multiples of it as well as the current nacelle position  $\Phi_{nacelle}$  are also drawn. The angles are relative to the non-moving inertial coordinate system of the CFD simulation. In the acoustic simulation, the blades and the tower were used both together and separately as emitters. The time offset of 3 s due to sound propagation over 1000 m is again compensated.

The tower emits almost equally loudly in all directions (omnidirectional) during normal operation of the WT, which is shown by the low dispersion of the highest peak sound pressure levels per time interval in Figure 12A. This is consistent with the numerical results of Klein<sup>9</sup> and Yauwenas et al.<sup>20</sup> Nevertheless, it becomes obvious that the loudest direction is permanently at about  $270^\circ$ , that is, on the side of the descending blade. The loudest frequency is almost always the second harmonic of the BPF. In the time range from 185 to 247 s in which the blades are

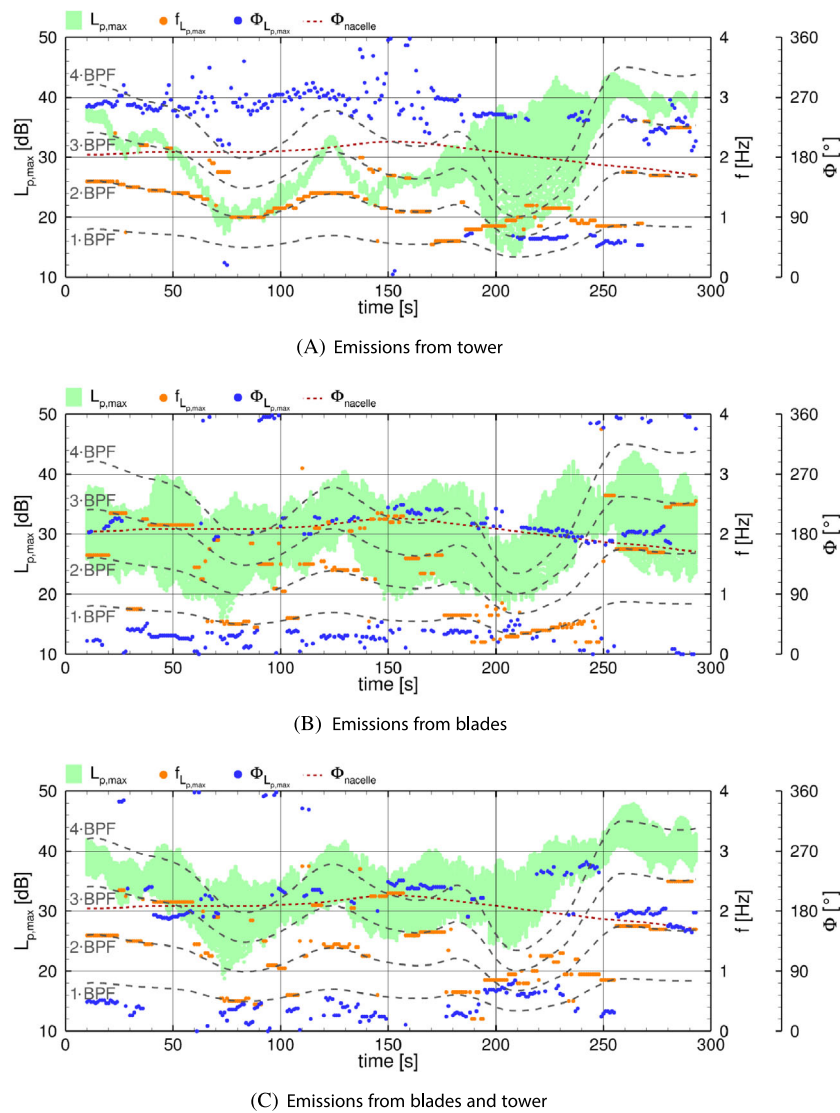


**FIGURE 12** Peak sound pressure level  $L_{p,max}$  of the loudest frequency for each observer on a circle around the WT from sliding 20-s intervals as well as the frequency  $f_{L_{p,max}}$  and position  $\phi_{L_{p,max}}$  relative to the WT of the loudest observer. In addition, the current nacelle position  $\phi_{nacelle}$  as well as the BPF and its harmonics are marked.

strongly pitched, the acoustic emission of the tower varies strongly over  $\phi$  (large dispersion of  $L_{p,max}$  per time interval). Also, the loudest frequency is no longer correlated with the rotational speed, confirming VS as the dominant noise source. The blades, on the other hand, have a pronounced directivity throughout the simulation period with persistent over 10 dB variation in  $L_{p,max}$  around the WT, as can be seen in Figure 12B. The highest peak sound pressure levels occur exclusively upstream ( $\phi \approx 180^\circ$ ) or downstream ( $\phi \approx 0^\circ / 360^\circ$ ) of the WT. The loudest frequency is also clearly correlated with the rotational speed but jumps constantly between the first four harmonics of the BPF. The section with heavily pitched blades is only noticeable by the fact that the loudest frequency constantly corresponds to the BPF. This is in line with the less impulsive interaction with the tower due to the lower blade speed. If the total emission of the WT, that is, of the blades and the tower together, is considered in Figure 12C, it can be seen that the loudest frequency and direction in normal operation behaves similarly to the emission of the blades, whereas in the pitched time section, the loudest sound emission comes from the tower, as it was also shown in Figure 8.

#### 4.3.3 | Transient noise emission effects

To qualitatively investigate the characteristics of the intermittent events as they occur during the extreme event, a continuous wavelet transform (CWT) is used. It allows a high frequency resolution at low frequencies and a high time resolution at higher frequencies. In contrast to the STFT,

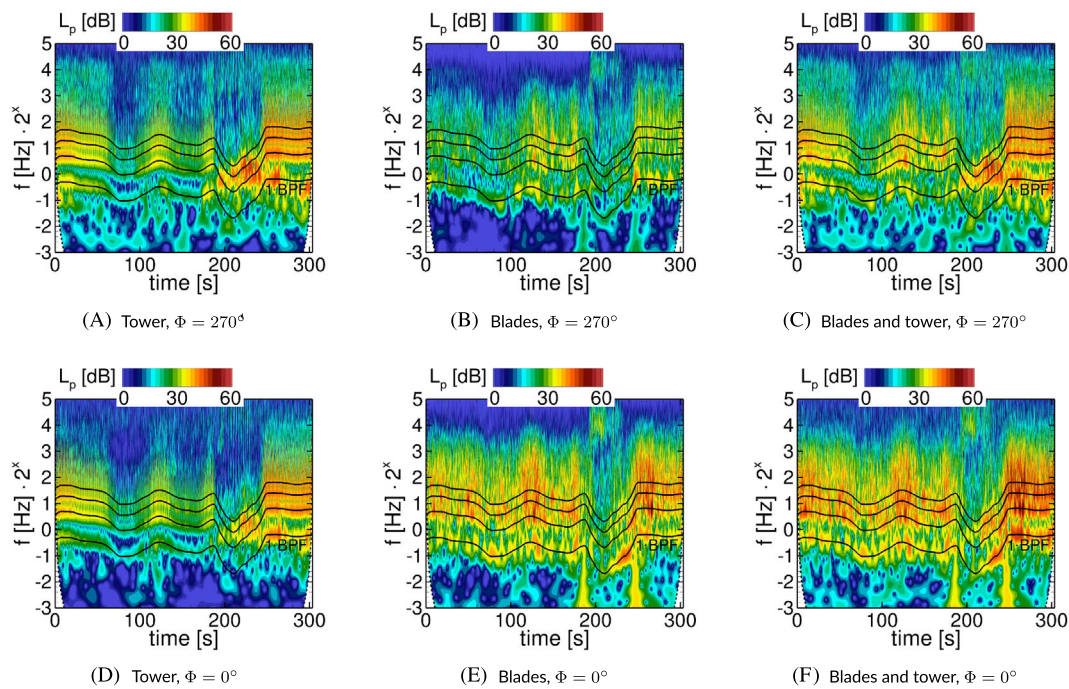


**FIGURE 13** Scalograms of the CWT of the sound pressure level  $L_p$  1000 m lateral and downstream of the WT.

the relative accuracy of the resolution of a frequency or a cycle in the frequency and time domain thus remains constant over the entire time-frequency range. The time signal is transformed with a Morlet wavelet, which has been shown to be the best choice for detecting helicopter blade vortex interaction noise,<sup>45</sup> which is very similar to BTI noise. Figure 13 shows scalograms for two observer positions, one lateral ( $\phi \approx 270^\circ$ ) and one downstream ( $\phi \approx 0^\circ$ ) of the WT. It is known from previous studies<sup>21,22</sup> that the emission characteristics of a WT differ significantly between crosswind and downwind/upwind direction. The first four harmonics of the BPF are plotted for reference. Comparing the Figure 13A,D, which represent the emitted spectra of the tower for the different directions, shows almost identical emission in normal mode. In load reduction mode, however, a significantly stronger sound emission occurs laterally in the frequency range 1–2 Hz, which matches the observation from Figure 12A regarding the VS. Otherwise, a clear dependence of the tower emissions with the BPF is observable, which, however, is more impulsive than sinusoidal in shape, as already shown in Wenz et al.<sup>22</sup> For the blades in Figure 13B,E, a less clear relationship with BPF is evident, and most importantly the pattern is less regular over time. This shows that a stochastic influence dominates, namely, the interaction with the inflow turbulence, with  $L_p$  being significantly higher downstream than lateral. In the total emission (Figure 13C,F), the patterns of the two emitters overlap and, depending on the time period and position, the blades or the tower dominate.

## 5 | CONCLUSION

In this study, a numerical process chain consisting of the meteorological model system *PALM*, the CFD solver *FLOWer*, the MBS software *SIMPACK* and the Ffowcs Williams-Hawkings code *ACCO* was used for the multidisciplinary simulation of a generic WT. A new aspect was the realization of a very complex operational behaviour with variable rotational speed, pitch angle and yaw. This enables the aerodynamic and aeroacoustic characterization of an entire WT in the turbulent atmosphere during a specific meteorological event, taking into account the structural deformations. With regard to the acoustic emission, it was possible to determine and analyse the influence of the operational management and the inflow parameters on the low-frequency noise.

The meteorological situation was selected with the intention of enforcing a control-intensive operation of the generic WT. The flow situation measured during a cold front passage in Harsewinkel, Germany, was reproduced with the meteorological model system *PALM* using a *nudging* approach to ensure a realistic wind field generation. The 5-min situation is characterized by a rapid change in wind direction, which the yaw controller cannot compensate for instantaneously. The generated spatial and temporal flow field was fed into the aero-servo-elastic CFD simulation with *FLOWer* via a Dirichlet boundary condition. In the MBS model in *SIMPACK*, the control of the WT operation was implemented via control laws. According to the power and the anemometer speed and direction, the rotational speed, the pitch angle and the nacelle position were variably controlled.

The situation results in three fundamentally different operating modes, the lower partial load range, a load reduction mode due to strong yawed inflow and operation close to full load. The rotational speed follows the wind speed unless the anemometer detects too strong a yawed inflow, which causes the pitch controller to turn the blades out of the wind to protect the WT, which also reduces the rotational speed. This happens because the yaw controller with  $0.4^\circ \text{ s}^{-1}$  is too slow to follow the wind rotation. The numerical simulation chain provides an aero-servo-elastically reasonable behaviour of the generic WT for this situation with the created setup.

The aeroacoustic evaluation shows that the emitted low-frequency sound power is primarily proportional to the rotational speed. The emissions from the tower react even more sensitively to changes than the blades. Since the rotational speed during normal operation up to the nominal speed is essentially depending directly on the wind speed, this is the dominant meteorological influencing quantity. In addition, the low-frequency sound emissions of the blades correlate with the turbulence intensity of the inflow. The yawed inflow, on the other hand, is not a significant parameter, unless it is so large that it causes a change of the operating mode to load reduction for the protection of the WT. Then a very low-frequency sound emission due to strong VS caused by a stable von Kármán vortex street occurs at the tower, which dominates over the blades. At full load, blades and tower emit with a similar sound power. In normal operation, the directivity of the tower is almost omnidirectional, independent of the flow and operating conditions. Only in load reduction mode there is a laterally enhanced emission due to the dominant VS. The directivity of the blades is completely independent of operation, with the strongest sound emission always normal to the rotor plane (downstream and upstream).

The results of the aero-servo-elastic CFD simulation in this study and its aeroacoustic evaluation show that:

- The numerical process chain allows the simulative reproduction of the WT response to very complex meteorological situations including realistic controller behaviour.
- The wind speed and, linked to it, the rotational speed as well as the turbulence intensity are the main influencing factors for the emitted low-frequency sound power of the WT.
- The directivity of the low-frequency sound emissions of the tower changes in load reduction mode, while that of the blades remains unchanged.

## AUTHOR CONTRIBUTIONS

Florian Wenz prepared the high-fidelity *FLOWer* setup, performed the CFD-MBS simulation, did the aeroacoustic evaluation and wrote the paper. Oliver Maas prepared and performed the meteorological *PALM* simulation. Matthias Arnold derived the generic I82, prepared the MBS model and identified the meteorological situation. Thorsten Lutz and Ewald Krämer initiated the research, supervised the work and revised the manuscript. All authors have read and agreed to the published version of the manuscript.

## ACKNOWLEDGEMENTS

The authors gratefully acknowledge the High Performance Computing Center Stuttgart (HLRS) for providing computational resources within the project WEALoads. Open Access funding enabled and organized by Projekt DEAL.

## CONFLICT OF INTEREST STATEMENT

The authors declare no conflict of interest.

## DATA AVAILABILITY STATEMENT

The raw data of the simulation results can be made available by contacting the corresponding author.

## ORCID

Florian Wenz  <https://orcid.org/0000-0002-4201-588X>

## PEER REVIEW

The peer review history for this article is available at <https://www.webofscience.com/api/gateway/wos/peer-review/10.1002/we.2826>.

## REFERENCES

1. Orlanski I. A rational subdivision of scales for atmospheric processes. *Bullet Am Meteorol Soc.* 1975;56(5):527-530.
2. Fischer B, Shan M. A survey on power control methods for ad hoc networks. IWES Project report 01/104256; 2013.
3. Jonkman J, Butterfield S, Musial W, Scott G. Definition of a 5-MW Reference Wind Turbine for Offshore System Development. 2009. <https://www.osti.gov/biblio/947422>
4. Popko W, Thomas P, Sevinc A, et al. IWES Wind Turbine IWT-7.5-164 Rev 4; 2018.
5. Bak C, Zahle F, Bitsche R, et al. The DTU 10-MW Reference Wind Turbine; 2013.



6. Gözcü O, Verelst DR. The effects of blade structural model fidelity on wind turbine load analysis and computation time. *Wind Energy Sci.* 2020;5(2): 503-517.
7. Li Y, Castro AM, Martin JE, Sinokrot T, Prescott W, Carrica PM. Coupled computational fluid dynamics/multibody dynamics method for wind turbine aero-servo-elastic simulation including drivetrain dynamics. *Renew Energy.* 2017;101:1037-1051.
8. Yang J, Fang L, Song D, et al. Review of control strategy of large horizontal-axis wind turbines yaw system. *Wind Energy.* 2021;24(2):97-115.
9. Klein L. Numerische Untersuchung aerodynamischer und aeroelastischer Wechselwirkungen und deren Einfluss auf tieffrequente Emissionen von Windkraftanlagen. *Dissertation: Universität Stuttgart*; 2020.
10. Wagner S, Bareiß R, Guidati G. *Wind Turbine Noise*. Berlin, Heidelberg: Springer Berlin Heidelberg; 1996. <https://doi.org/10.1007/978-3-642-88710-9>
11. Delfs J. *Basics of Aeroacoustics: Lecture notes*, Technische Universität Braunschweig; 2019. [https://www.dlr.de/as/Portaldaten/5/Resources/dokumente/abteilungen/abt\\_ta/Notes\\_Basics\\_of\\_Aeroacoustics\\_Delfs\\_19\\_20.pdf](https://www.dlr.de/as/Portaldaten/5/Resources/dokumente/abteilungen/abt_ta/Notes_Basics_of_Aeroacoustics_Delfs_19_20.pdf)
12. Sengupta TK, Bhumkar YG. *Computational Aerodynamics and Aeroacoustics*: Springer Singapore; 2020. <https://doi.org/10.1007/978-981-15-4284-8>
13. Liu WY. A review on wind turbine noise mechanism and de-noising techniques. *Renew Energy.* 2017;108:311-320.
14. Keith SE, Daigle GA, Stinson MR. Wind turbine low frequency and infrasound propagation and sound pressure level calculations at dwellings. *The J Acoust Soc Am.* 2018;144(2):981-996. <https://doi.org/10.1121/1.5051331>
15. Blumendeller E, Kimmig I, Huber G, Rettler P, Cheng PW. Investigations on low frequency noises of on-shore wind turbines. *Acoustics.* 2020;2(2): 343-367.
16. Hansen CH, Hansen KL. Recent Advances in Wind Turbine Noise Research. *Acoustics.* 2020;2(1):171-206.
17. D'Amico S, Van Renterghem T, Botteldooren D. Influence of atmospheric conditions on measured infrasound from wind turbines. *J Wind Eng Ind Aerodyn.* 2022;225(November 2021):105021. <https://doi.org/10.1016/j.jweia.2022.105021>
18. Lighthill MJ. On sound generated aerodynamically I. General theory. *Proc Royal Soc London. Ser A. Math Phys Sci.* 1952;211(1107):564-587. <https://doi.org/10.1098/rspa.1952.0060>
19. Ffowcs Williams JE, Hawkings DL. Sound generation by turbulence and surfaces in arbitrary motion. *Phil Trans Royal Soc London. Ser A, Math Phys Sci.* 1969;264(1151):321-342. <https://doi.org/10.1098/rsta.1969.0031>
20. Yauwenas Y, Zajamšek B, Reizes J, Timchenko V, Doolan C. Directivity of blade-tower interaction noise. *JASA Express Lett.* 2021;1(6):63601.
21. Klein L, Gude J, Wenz F, Lutz T, Krämer E. Advanced computational fluid dynamics (CFD) multi-body simulation (MBS) coupling to assess low-frequency emissions from wind turbines. *Wind Energy Sci.* 2018;3(2):713-728.
22. Wenz F, Lutz T, Krämer E. Impact of turbulent inflow and orography on the low-frequency noise sources of a wind turbine. *J Phys: Conf Ser.* 2022; 2265:32060.
23. Cheng Z, Lien FS, Yee E, Meng H. A unified framework for aeroacoustics simulation of wind turbines. *Renew Energy.* 2022;188:299-319.
24. Wenz F, Langner J, Lutz T, Krämer E. Impact of the wind field at the complex-terrain site Perdigoão on the surface pressure fluctuations of a wind turbine. *Wind Energy Sci.* 2022;7(3):1321-1340.
25. Maronga B, Banzhaf S, Burmeister C, et al. Overview of the PALM model system 6.0. *Geosci Model Develop.* 2020;13(3):1335-1372. <https://gmd.copernicus.org/articles/13/1335/2020/>
26. Kroll N, Rossow CC, Becker K, Thiele F. The MEGAFLOW project. *Aerospace Sci Technol.* 2000;4(4):223-237.
27. Kowarsch U, Keßler M, Krämer E. High order CFD-simulation of the rotor-fuselage interaction. 39th European Rotorcraft Forum, Moscow; 2013.
28. Weihing P, Letzgus J, Bangga G, Lutz T, Krämer E. Hybrid RANS/LES Capabilities of the Flow Solver FLOWer-Application to Flow Around Wind Turbines. *Progr Hybrid RANS-LES Model.* 2018;2018:369-380.
29. Meister K. *Numerische Untersuchung zum aerodynamischen und aeroelastischen Verhalten einer Windenergieanlage bei turbulenter atmosphärischer Zuströmung*: Shaker Verlag; 2015.
30. Luhmann B, Seyedin H, Cheng PW. Aero-structural dynamics of a flexible hub connection for load reduction on two-bladed wind turbines. *Wind Energy.* 2017;20:521-535.
31. Guma G, Bangga G, Lutz T, Krämer E. Aeroelastic analysis of wind turbines under turbulent inflow conditions. *Wind Energy Sci.* 2021;6(1):93-110.
32. Keßler M, Wagner S. Source-time dominant aeroacoustics. *Comput Fluids.* 2004;33(5-6):791-800.
33. Ghasemian M, Nejat A. Aerodynamic noise prediction of a Horizontal Axis Wind Turbine using Improved Delayed Detached Eddy Simulation and acoustic analogy. *Energy Convers Manag.* 2015;99:210-220. <https://doi.org/10.1016/j.enconman.2015.04.011>
34. Arnold M, Wenz F, Kühn T, Lutz T, Altmikus A. Integration of system level CFD simulations into the development process of wind turbine prototypes. *J Phys: Confer Ser.* 2020;1618:5.
35. Anthes RA. Data assimilation and initialization of hurricane prediction models. *Int J Atmos Sci.* 1974;31(3):702-719. [http://journals.ametsoc.org/doi/10.1175/1520-0469\(1974\)031%3C0702:DA%AIOH%3E2.0.CO;2](http://journals.ametsoc.org/doi/10.1175/1520-0469(1974)031%3C0702:DA%AIOH%3E2.0.CO;2)
36. Neggars RAJ, Siebesma AP, Heus T. Continuous single-column model evaluation at a permanent meteorological supersite. *Bullet Am Meteorol Soc.* 2012;93(9):1389-1400.
37. Kühn T, Altmikus A, Lutz T, Schwarz T, Raasch S, Thiele F. *AssiSt—Anlagen-Strömungssimulation und Standortkalibrierung: Schlussbericht*: WRD Wobben Research and Development GmbH; 2018. <https://www.tib.eu/de/suchen/id/TIBKAT%3A1029338604>
38. Sayed M, Lutz T, Krämer E. Aerodynamic investigation of flow over a multi-megawatt slender bladed horizontal-axis wind turbine. In: *Renewable Energies Offshore - 1st International Conference on Renewable Energies Offshore, RENEW 2014*; 2015:773-780.
39. Spalart PR, Deck S, Shur ML, Squires KD, Strelets MK, Travin A. A new version of detached-eddy simulation, resistant to ambiguous grid densities. *Theor Comput Fluid Dyn.* 2006;20(3):181-195.
40. Gritskevich MS, Garbaruk AV, Menter FR. Fine-tuning of DDES and IDDES formulations to the  $k-\omega$  shear stress transport model. *Progr Flight Phys.* 2013;5:23-42.
41. Matha D, Stefan H, Thomas H. *Methodology and Results of Loads Analysis of Wind Turbines with Advanced Aeroelastic Multi-body Simulation*. DEWEK, Bremen 2010; 2010.
42. IEC 61400-1:2019. *Wind Turbines Part 1: Design Requirements*: International Electrotechnical Commission; 2019.
43. Hart E, Guy C, Tough F, Infield D. Wind site turbulence de-trending using statistical moments: Evaluating existing methods and introducing a Gaussian process regression approach. *Wind Energy.* 2021;24(9):1013-1030.

44. Larsen GC, Hansen KS. De trending of wind speed variance based on first order second order statistical moments only. *Wind Energy*. 2014;17(12):1905-1924. <https://doi.org/10.1002/we.1676>
45. Stephenson JH, Tinney CE. Extracting blade-vortex interactions using continuous wavelet transforms. *J Am Helicopter Soc*. 2017;62(2):1-10.

**How to cite this article:** Wenz F, Maas O, Arnold M, Lutz T, Krämer E. Assessment of low-frequency aeroacoustic emissions of a wind turbine under rapidly changing wind conditions based on an aero-servo-elastic CFD simulation. *Wind Energy*. 2023;26(8):745-762. doi:10.1002/we.2826

## APPENDIX A: ANEMOMETER CORRECTION

The yaw controller of the I82 from Arnold et al<sup>34</sup> requires the position of the nacelle relative to the wind direction. As with a real wind turbine, this information must be derived from the flow situation recorded at the anemometer. However, the flow field at the anemometer position is strongly influenced by the WT. It includes the blade root wake that periodically hits the anemometer and the rotor blockage.

In Figure A1, the uncorrected anemometer signals, as extracted from the *FLOWer* simulation, can be seen, in terms of the wind speed  $u_h$  and the wind direction  $\Delta\phi$ . These signals are low-pass filtered in the controller to filter out the blade wake. However, this is not yet sufficient to capture the actual inflow (the wind field without WT influence). The swirl in the wake of the rotor as well as the deceleration of the flow due to induction must be compensated. This is done by means of calibrated correction factors for each point of operation.<sup>34</sup>

Comparing the corrected anemometer signals of the controller in *SIMPACK* for both velocity and direction with the corresponding graphs from the CFD simulation without WT in Figure A1, some deviations can be seen. The apparent time offset results from the application of a delay element (PT1 element) in the controller to smooth the signal in combination with the reduced flow velocity due to the blockage of the WT. This cannot be prevented without additional measuring systems, such as a hub lidar, which measure the flow upstream of the WT. The offset in the amplitudes, however, result from the correction factors. They are determined in Arnold et al<sup>34</sup> from unsteady CFD simulations with different constant homogeneous inflows. In the context of the simulation from the present work, it can be seen that the correction factors do not depend exclusively on the wind speed, but need to be adjusted for turbulent or yawed inflow. This conclusion results from the adequate correction at full load operation from 245 s, for which  $TI$  and  $\Delta\phi$  are low, while especially in situations with non-stationary operation (180 to 245 s) the correction is inaccurate.

For the simulation in this work, the inaccurate correction curves only have consequences in the time range from 180 to 245 s, where the pitch increase is unnecessarily strong. During the rest of the simulation, the controller does not use anemometer data.

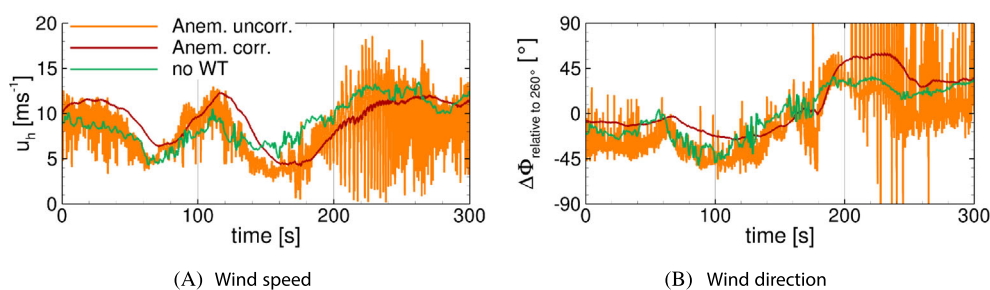


**FIGURE A1** Wind speed  $u_h$  and direction  $\Delta\phi$  simulated with *FLOWer* at the anemometer, uncorrected, after correction and as a reference from the simulation without WT.